linearly dependent on ν. When electrostatic interactions up to the third-neighbour shells are included, these charged planes generate internal electric fields whose directions are those of Fig. 1 and whose magnitudes are linearly dependent on ν.) Increasing ν thus results in stronger internal fields with opposite directions. These strong opposite fields tend to suppress the polarization's component along the direction of compositional modulation. As a result, u_z becomes smaller than u_x and u_y. The studied structures with intermediate values of ν thus first undergo a paraelectric-to-orthorhombic ferroelectric transition at high temperature before adopting the monoclinic M_B phase for ground state. The modulated structures with the largest values of ν have the strongest internal electric fields, which annihilate u_z at any temperature. Consequently, such structures never reach the monoclinic phase and instead adopt the orthorhombic phase for ground state. The large values of d_{34} and χ_{33} shown in Figs 2 and 3 simply reflect the considerable change of u_z when some parameters are slightly modified (ν at a fixed temperature, or T for a fixed value of ν), especially for structures at the borderline between the monoclinic and orthorhombic phases. In other words, the large electromechanical responses are consistent with the ease of rotating the polarization[7,16]. We have shown here results for the thinnest possible structures. For larger structures, with thicker layers, the 'unusual' electromechanical responses will be smaller due to smaller internal electric fields.

On the basis of the electrostatic considerations discussed above, we expect that any alloy made of heterovalent atoms and with a rhombohedral ground state in its disordered form should have the structural, piezoelectric and dielectric anomalies displayed in Figs 2 and 3, when the atomic ordering along the [001] direction is adjusted in a certain way. The atomically ordered structures discussed here could be grown by means of a pulse laser deposition technique[17] or by using molecular beam epitaxy. □

1. Abe, K. & Komatsu, S. Ferroelectric properties in epitaxially grown $Ba_xSr_{1-x}TiO_3$ thin films. *J. Appl. Phys.* **77,** 6461–6465 (1995).
2. Uchino, K. *Piezoelectric Actuators and Ultrasonic Motors* (Kluwer Academic, Boston, 1996).
3. Sai, N., Meyer, B. & Vanderbilt, D. Compositional inversion symmetry breaking in ferroelectric perovskites. *Phys. Rev. Lett.* **84,** 5636–5639 (2000).
4. Park, S.-E. & Shrout, T. R. Ultrahigh strain and piezoelectric behavior in relaxor based ferroelectric single crystal. *J. Appl. Phys.* **82,** 1804–1811 (1997).
5. Service, R. F. Shape-changing crystals get shiftier. *Science* **275,** 1878 (1997).
6. Noheda, B. *et al.* A monoclinic ferroelectric phase in the $Pb(Zr_{1-x}Ti_x)O_3$ solid solution. *Appl. Phys. Lett.* **74,** 2059–2061 (1999).
7. Bellaiche, L., García, A. & Vanderbilt, D. Finite-temperature properties of $Pb(Zr_{1-x}Ti_x)O_3$ alloys from first principles. *Phys. Rev. Lett.* **84,** 5427–5430 (2000).
8. Hemphill, R., Bellaiche, L., García, A. & Vanderbilt, D. Finite-temperature properties of disordered and ordered $Pb(Sc_{0.5}Nb_{0.5})O_3$ alloys. *Appl. Phys. Lett.* **77,** 3642–3644 (2000).
9. Hohenberg, P. & Kohn, W. Inhomogeneous electron gas. *Phys. Rev.* **136,** B864–871 (1964).
10. Kohn, W. & Sham, L. J. Self-consistent equations including exchange and correlation effects. *Phys. Rev.* **140,** A1133–1138 (1965).
11. Vanderbilt, D. Soft self-consistent pseudopotentials in a generalized eigenvalue formalism. *Phys. Rev. B* **41,** 7892–7895 (1990).
12. Bellaiche, L. & Vanderbilt, D. Virtual crystal approximation revisited: Application to dielectric and piezoelectric properties of perovskites. *Phys. Rev. B* **61,** 7877–7882 (2000).
13. Chu, F., Reaney, I. M. & Setter, N. Spontaneous (zero-field) relaxor-to-ferroelectric-phase transition in disordered $Pb(Sc_{1/2}Nb_{1/2})O_3$. *J. Appl. Phys.* **77,** 1671–1676 (1995).
14. Vanderbilt, D. & Cohen, M. H. Monoclinic and triclinic phases in higher-order Devonshire theory. *Phys. Rev. B* **63,** 094108 (2001).
15. Ramer, N. J. & Rappe, A. M. Application of a new virtual crystal approach for the study of disordered perovskites. *J. Phys. Chem. Solids* **61,** 315–320 (2000).
16. Fu, H. & Cohen, R. E. Polarization rotation mechanism for ultrahigh electromechanical response in single crystal piezoelectrics. *Nature* **403,** 281–283 (2000).
17. Brazier, M., McElfresh, M. & Mansour, S. Unconventional hysteresis behavior in compositionally graded $Pb(Zr,Ti)O_3$ thin films. *Appl. Phys. Lett.* **72,** 1121–1123 (1998).

Elasticity of iron at the temperature of the Earth's inner core

Gerd Steinle-Neumann*, Lars Stixrude*, R. E. Cohen† & Oguz Gülseren‡

* Department of Geological Sciences, University of Michigan, Ann Arbor, Michigan 48109-1063, USA
† Carnegie Institution of Washington and Center for High Pressure Research, Washington DC 20015-1305, USA, and Seismological Laboratory, California Institute of Technology, Pasadena, California 91125, USA
*‡ NIST Center for Neutron Research, National Institute of Standards and Technology, Gaithersburg, Maryland 20899-8562 USA, and Department of Material Sciences and Engineering, University of Pennsylvania, Philadelphia, Pennsylvania 19104, USA*

....

Seismological body-wave[1] and free-oscillation[2] studies of the Earth's solid inner core have revealed that compressional waves traverse the inner core faster along near-polar paths than in the equatorial plane. Studies have also documented local deviations from this first-order pattern of anisotropy on length scales ranging from 1 to 1,000 km (refs 3, 4). These observations, together with reports of the differential rotation[5] of the inner core, have generated considerable interest in the physical state and dynamics of the inner core, and in the structure and elasticity of its main constituent, iron, at appropriate conditions of pressure and temperature. Here we report first-principles calculations of the structure and elasticity of dense hexagonal close-packed (h.c.p.) iron at high temperatures. We find that the axial ratio c/a of h.c.p. iron increases substantially with increasing temperature, reaching a value of nearly 1.7 at a temperature of 5,700 K, where aggregate bulk and shear moduli match those of the inner core. As a consequence of the increasing c/a ratio, we have found that the single-crystal longitudinal anisotropy of h.c.p. iron at high temperature has the opposite sense from that at low temperature[6,7]. By combining our results with a simple model of polycrystalline texture in the inner core, in which basal planes are partially aligned with the rotation axis, we can account for seismological observations of inner-core anisotropy.

Although the inner core is probably not pure iron, the amount of light alloying element is small (2 to 3% mass fraction)[8] and may have a correspondingly small effect on elasticity[8]. The experimentally determined low-temperature, high-pressure phase of iron at least up to 300 GPa is h.c.p. (ϵ-phase)[9]. This is also the liquidus phase up to at least 100 GPa (ref. 10), and there is theoretical evidence[8,11] that h.c.p. is the stable phase at inner-core conditions. Some experiments have been interpreted as indicating a different phase at high temperature and pressure[12–14], but the evidence is inconclusive[15], and the proposed structures[13,14] are closely related to h.c.p.

Despite the importance for our understanding of inner-core structure, the elastic-constant tensor of h.c.p. iron at the relevant pressure and temperature is currently unknown. Experimental measurements of the full elastic-constant tensor are so far restricted to ambient temperature. The isotropically averaged bulk and shear modulus at the pressure of the inner-core boundary and a temperature of 5,400 K has been reported[16], but the full elastic-constant tensor at these conditions was not determined. The method of ref. 16, while promising, does not treat the electronic structure from first principles. Instead, an effective-potential model fit to short *ab initio* molecular dynamics trajectories is used. Calculations of the elastic constants with *ab initio* molecular dynamics may not currently be feasible, because long trajectories are required to obtain converged values from the relevant fluctuation formulas.

To overcome these limitations, we have developed a method that combines a first-principles treatment of the electronic structure
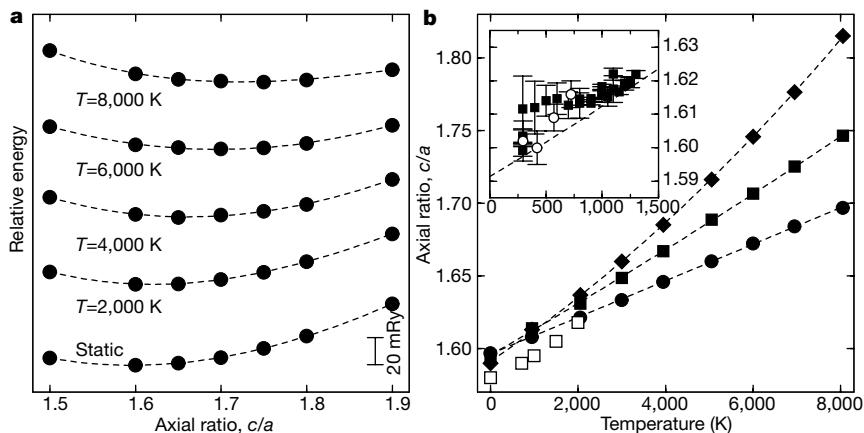
Figure 1 Structure of h.c.p. iron at high pressure as a function of temperature. **a**, Relative energies (F) for a density of 13.04 Mg m^{-3} as a function of axial ratio c/a for various temperatures. The scale bar refers to strain energy differences only. **b**, The axial ratio c/a as a function of temperature for three different densities (filled diamonds, 12.52 Mg m^{-3}; filled squares, 13.04 Mg m^{-3}; filled circles, 13.62 Mg m^{-3}); dashed lines are quadratic fits to the results. Open squares, previous theoretical work[17] at 13.04 Mg m^{-3}. Inset, comparison of our results at the lowest density (static pressure of 190 GPa, dashed line) with a polybaric set of experimental data at lower pressures. Open circles, data from ref. 19 (15–20 GPa); filled squares, data from ref. 20 (23–35 GPa).

with an efficient model of the lattice vibrations that allows fully converged computations of the high-temperature elastic constants. Thermodynamic properties are governed by the Helmholtz free energy F as a function of volume (V) and temperature (T)

$$F(V,T) = E_0(V) + E_{el}(V,T) - TS_{el}(V,T) + F_{vib}(V,T) \quad (1)$$

where $E_0(V)$ is the static total energy, $E_{el}(V,T)$ the contribution due to thermal excitations of the electrons, $S_{el}(V,T)$ the electronic entropy, and $F_{vib}(V,T)$ the phonon contribution. We obtain the first three terms on the right-hand side of equation (1) by an all-electron method (the linearized augmented plane wave method, LAPW), calculating $E_{band} = E_0 + E_{el}$ directly and evaluating the Fermi–Dirac occupation of the electronic states for S_{el}. $F_{vib}(V,T)$ is obtained using the particle-in-a-cell model[17]: this is a classical mean-field approach to lattice vibrations, in which one atom (the wanderer) is moved in the potential of the otherwise fixed lattice. The cell model includes intrinsic anharmonicity, which is important at the extreme conditions of the inner core. The factorized canonical partition function for F_{vib} is evaluated by computing the change in the electronic free energy $F_{el}(V,T) = E_{el}(V,T) - TS_{el}(V,T)$ of a 48-atom supercell as a function of displacement of the wanderer along special symmetry directions[17].

For efficient calculations of the energetics of the wanderer, we use a plane wave mixed basis method (PWMB). The use of a mixed basis, which contains localized basis functions in addition to plane waves, means that we are able to use harder pseudopotentials than are typical. Our Troullier–Martins pseudopotentials treat 3s, 3p and 3d states as valence states. Calculations based on harder pseudopotentials are expected to more nearly capture the all-electron limit: we reproduce pressures from the LAPW results at inner-core density to within 1%, and the elastic constants to within 2% r.m.s. The cell model has successfully been applied to calculations of thermodynamic properties of iron, including the Hugoniot up to inner-core densities[17], as well as high-temperature thermodynamics of tantalum, including elastic constants[18].

We obtain the equilibrium structure of h.c.p. iron over a range of densities and temperatures that span those of the inner core by computing F for a number of different values of c/a and determining the minimum free-energy value (Fig. 1a). We compute the full elastic-constant tensor by applying small magnitude finite strains to the lattice and evaluating the resulting changes in $F(V,T)$. By using volume-conserving strains, we assure the identity of the elastic constants calculated as thermodynamic variables with the stress–strain coefficients that are appropriate for elastic wave propagation[7].

We find that the ratio c/a in h.c.p. iron changes considerably with temperature (Fig. 1): for a density of 13.04 Mg m^{-3}, this ratio increases from slightly less than the ideal value defined by hard-sphere packing (1.633) at low temperature to more than 1.7 at 6,000 K (Fig. 1b). This behaviour has been recognized before in experiments at lower pressure[19,20] and in calculations[17], but is neglected in some recent theoretical work[11,21].

The change in c/a with temperature is important, because it has a direct influence on the elastic anisotropy. As the c-axis expands with increasing temperature (at constant density), it becomes softer (more compressible). The corresponding longitudinal modulus, c_{33}, softens sufficiently that it becomes smaller than the other

Table 1 Elastic moduli of dense h.c.p. iron at high temperatures

T	c_{11} (GPa)	c_{12} (GPa)	c_{13} (GPa)	c_{33} (GPa)	c_{44} (GPa)	c_{66} (GPa)	K_S (GPa)	μ (GPa)	σ
0	1,880	880	770	2,065	450	500	1,185	505	0.31
4,000	2,035 (2,045)	1,435 (1,445)	810 (855)	1,650 (1,835)	270	300	1,325	335	0.38
5,000	2,050 (2,065)	1,720 (1,735)	860 (910)	1,555 (1,760)	210	165	1,375	240	0.42
6,000	2,130 (2,150)	2,010 (2,030)	925 (990)	1,470 (1,685)	140	60	1,425	145	0.45
Inner core							1,400	170	0.44

Elastic constants for h.c.p. iron calculated at a density of 13.04 Mg m^{-3} (V = 48 bohr^3 per atom) at various temperatures. We calculate the Helmholtz free energy (equation (1)) by combining LAPW results for the electronic terms and a particle-in-a-cell model for the phonon contribution (see text). Computational parameters for the LAPW calculations are given in ref. 7. For the particle-in-a-cell method we evaluate the energetics of a wanderer atom in a 48-atom supercell with a Brillouin zone sampling of 8 k-points. To efficiently perform calculations for the wanderer displacement, we use a PWMB method with energy cut-offs of 1,400 eV and 80 eV in the muffin-tin spheres and the interstitial region, respectively. In the PWMB method we use Troullier–Martins pseudopotentials which are constructed using 3s, 3p and 3d as valence states (3d local) with cut-off radii of 1.5 bohr to avoid pseudopotential overlap at the small unit cell volume of this study. $c_{66} = 1/2(c_{11} - c_{12})$ is a shear elastic constant and added for comparison with c_{44}. Isothermal elastic constants are converted to adiabatic constants (shown in parentheses) using thermodynamic derivatives of $F(V,T)$. They are calculated self-consistently from our results. Adiabatic aggregate moduli K_S, μ and Poisson's ratio (σ) are given for comparison with seismic properties of the inner core at the same density (ref. 24).

longitudinal modulus c_{11} (Fig. 2a). As a result, the sense of the longitudinal anisotropy is reversed at high temperature, with compressional acoustic wave propagation being faster in the basal plane than along the c axis (Fig. 2b). The off-diagonal elastic constants are also affected by the temperature-induced change in structure: c_{12} increases rapidly with temperature, because the basal plane shrinks with increasing temperature at constant density. The shear constants c_{44} and $c_{66} = 1/2(c_{11} - c_{12})$ show a strong temperature dependence, and decrease by a factor of almost four at 6,000 K and change order as well (Fig. 2a). As a result, the velocity of shear waves is considerably smaller at high temperature and the sense of shear anisotropy is reversed (Fig. 2b), with the propagation of the (001) polarized shear wave becoming faster along the c-axis than in the basal plane. In agreement with ref. 16, our calculations imply a shear instability in h.c.p. iron at very high temperature (c_{66} approaches zero at 7,000 K).

The temperature-induced reversal in longitudinal anisotropy that we find would not have been predicted on the basis of the behaviour of other h.c.p. transition metals. At ambient pressure, many h.c.p. transition metals show little change in the ratio c_{11}/c_{33} with temperature: titanium shows the largest such change, with a decrease of 13% up to a temperature of 1,075 K, about half its melting point. Our results suggest that absolute temperature rather than the temperature relative to melting controls anisotropy. The character-

istics of elasticity we find at high temperature invalidate previous attempts to explain inner-core anisotropy using low-temperature elastic constants of iron[6,22,23].

To compare our results with seismological observations, we convert the computed isothermal elastic constants to adiabatic elastic constants, and from these we calculate the adiabatic bulk modulus (K_S) and shear modulus (μ) using Hashin–Shtrikman bounds (Fig. 3a, Table 1). The aggregate moduli we determine agree with those of the inner core at a temperature of 5,700 K. Poisson's ratio at 5,700 K (0.44) is in excellent agreement with previous theoretical estimates[16], and with the seismologically determined value for the inner core[24]. This shows that the high Poisson's ratio of the inner core can be accounted for by the effects of temperature and pressure on the elasticity of iron alone; it is unnecessary to invoke shear attenuation and dispersion or the presence of partial melt in the inner core, as has been suggested[22].

As the inner core is nearly isothermal[8], the comparison of K_S and μ to those determined seismologically for the inner core provides a way to estimate the temperature in the Earth's deep interior. This approach is complementary to estimates based on the melting temperature of iron, which suffer uncertainty due to the unknown but possibly large influence of light alloying elements[15,16,21]. Assuming a melting point depression of a few hundred degrees[15], our value for inner-core temperature of 5,700 K is consistent with estimates of the melting point of pure iron[21] (6,400 K) and of the Hugoniot in shock wave experiments (5,000 to 5,700 K at 245 GPa)[12]. The theoretical result of ref. 16 (5,400 K) and the extrapolated melting curve from static experiments[15] (~5,000 K) are both somewhat lower.
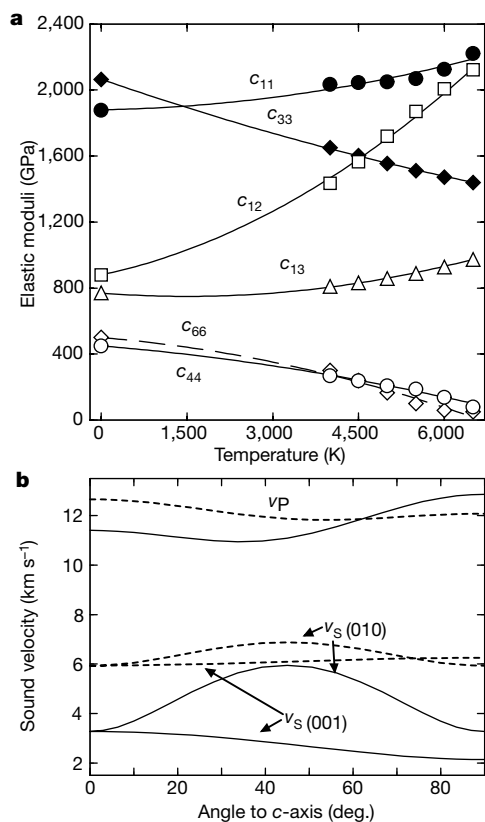
Figure 2 Elasticity of h.c.p. iron at a density of 13.04 Mg m^{-3}. **a**, Single-crystal elastic constants as a function of temperature. Static values are connected to the high-temperature results with a quadratic fit (solid lines). Data are shown for the longitudinal elastic constants c_{11} (filled circles) and c_{33} (filled diamonds), the off-diagonal constants c_{12} (squares) and c_{13} (triangles), and the shear elastic constants c_{44} (circles) and c_{66} (diamonds). $c_{66} = 1/2(c_{11} - c_{12})$ (dashed line) is not an independent elastic constant but is included for comparison with c_{44}. **b**, Acoustic anisotropy in the single crystal: wave velocities for the compressional wave (v_P) and the two polarizations of the shear wave (v_S, polarization direction indicated in brackets) are shown as a function of propagation direction with respect to the c-axis. Results at 6,000 K (solid lines) are compared to static results (dashed lines).
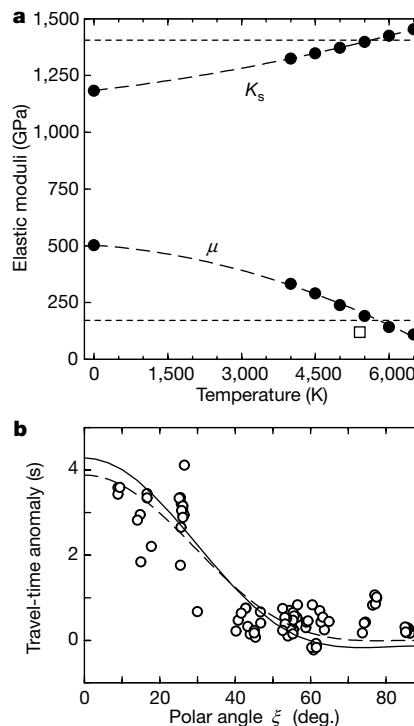
Figure 3 Acoustic properties of iron and the inner core. **a**, Comparison of iron's adiabatic bulk modulus (K_S) and shear modulus (μ) as a function of temperature (filled symbols, long-dashed lines) with the values of the inner core at the same density (13.04 Mg m^{-3}) (short-dashed lines, ref. 24). For comparison a previous theoretical result (open square, ref. 16) is included. **b**, The differential travel-time anomaly between BC and DF branches of the PKP core seismic phases due to inner-core anisotropy as a function of propagation direction. Our result (solid line) is for a model of the inner core in which 1/3 of the crystals have their basal planes aligned with the rotation axis. The observations of ref. 1 (open circles and dashed line) are shown for comparison. We convert from anisotropy in P-wave velocity for our model to differential travel time as outlined in ref. 6.

The sense of anisotropy that we find at high temperature changes our view of the polycrystalline texture of the inner core and the dynamic processes that may produce it. On the basis of our results, we propose a simple model of the polycrystalline texture of the inner core that explains the main features of its anisotropy. We find that if one-third of the basal planes are aligned with the Earth's rotation axis in an otherwise random medium, compressional wave travel-time anomalies are well explained (Fig. 3b). This model is almost certainly over-simplified. The key element is the tendency for the fast crystallographic direction (*a*) to be aligned with the observed symmetry axis of inner-core anisotropy (approximately polar). It is probable that the actual direction and degree of crystallographic alignment will vary with geographic location. Such variations may account for seismological observations of heterogeneity[3,4].

Important remaining questions include the origin of polycrystalline texture in the inner core, which may have been acquired during solidification of the inner core[25] or may have developed subsequently as a result of plastic deformation. If plastic deformation is the prevalent mechanism, the texture must depend on the dominant microscopic deformation mechanisms in iron at inner-core conditions and the source of stress that leads to the preferred alignment. While these are currently unknown, our simple textural model is consistent with the available information.

Candidates for the deformation mechanism include diffusion[23] and dislocation glide[26,27]. Among the crystallographic slip planes that may participate in dislocation glide, the basal plane is the easiest, according to recent experimental work[27]. The temperature-induced increase in c/a that we find may make basal slip even more favourable at high temperature. Several sources of the external stress field have been proposed: it may arise from aspherical growth of the inner core[23], gravitational coupling with the Earth's mantle[28], thermal convection in the inner core[26], or Maxwell stresses created by the Earth's magnetic field[29,30]. The pattern of flow in each of these cases is distinct; many models, however, share a polar-dominated flow, that is, a pattern of flow in which the highest velocities are oriented parallel to the polar axis.

If dislocation glide is the most important deformation mechanism, the easiest glide plane would be preferentially aligned with the dominant direction of flow, parallel to the rotation axis of the Earth. If diffusion dominates, preferred alignment is driven by minimization of strain energy, in which case the elastically stiffest (fastest) direction is aligned with the rotation axis[23]. In either case, basal planes would tend to be aligned with the pole, consistent with our simple textural model.   □

1. Song, X. D. & Helmberger, D. V. Anisotropy of the Earth's inner core. *Geophys. Res. Lett.* **20,** 2591–2594 (1993).
2. Tromp, J. Support for anisotropy of the Earth's inner core from free oscillations. *Nature* **366,** 678–681 (1993).
3. Vidale, J. E. & Earle, P. S. Fine scale heterogeneity in the Earth's inner core. *Nature* **404,** 273–275 (2000).
4. Creager, K. C. Large-scale variations in inner core anisotropy. *J. Geophys. Res.* **104,** 23127–23139 (1999).
5. Song, X. D. & Richards, P. G. Seismological evidence for differential rotation of the Earth's inner core. *Nature* **382,** 221–224 (1996).
6. Stixrude, L. & Cohen, R. E. High-pressure elasticity of iron and anisotropy of Earth's inner core. *Science* **267,** 1972–1975 (1995).
7. Steinle-Neumann, G., Stixrude, L. & Cohen, R. E. First-principles elastic constants for the hcp transition metals Fe, Co, and Re at high pressure. *Phys. Rev. B* **60,** 791–799 (1999).
8. Stixrude, L., Wasserman, E. & Cohen, R. E. Composition and temperature of the Earth's inner core. *J. Geophys. Res.* **102,** 24729–24739 (1997).
9. Mao, H.-K., Wu, Y., Chen, Y., Shu, J. F. & Jephcoat, A. P. Static compression of iron to 300 GPa and Fe$_{0.8}$Ni$_{0.2}$ alloy to 260 GPa: implications for composition of the core. *J. Geophys. Res.* **95,** 21737–21742 (1990).
10. Shen, G., Mao, H.-K., Hemley, R. J., Duffy, T. S. & Rivers, M. L. Melting and crystal structure of iron at high pressures and temperatures. *Geophys. Res. Lett.* **25,** 373–376 (1998).
11. Vočadlo, L. *et al.* Ab initio free energy calculations on the polymorphs of iron at core conditions. *Phys. Earth Planet. Inter.* **117,** 123–137 (2000).
12. Brown, J. M. & McQueen, R. Phase transitions, Grüneisen parameter, and elasticity for shocked iron between 77 GPa and 400 GPa. *J. Geophys. Res.* **91,** 7485–7494 (1986).
13. Dubrovinsky, L. S. *et al.* In situ X-ray study of thermal expansion and phase transition of iron at multimegabar pressure. *Phys. Rev. Lett.* **84,** 1720–1724 (2000).
14. Andrault, D., Fiquet, G., Kunz, M., Visocekas, F. & Häusermann, D. The orthorhombic structure of iron: an in situ study at high-temperature and high-pressure. *Science* **278,** 831–834 (1997).
15. Boehler, R. High-pressure experiments and the phase diagram of lower mantle and core materials. *Rev. Geophys.* **38,** 221–245 (2000).
16. Laio, A., Bernard, S., Chiarotti, G. L., Scandolo, S. & Tosatti, E. Physics of iron at Earth's core condition. *Science* **287,** 1027–1030 (2000).
17. Wasserman, E., Stixrude, L. & Cohen, R. E. Thermal properties of iron at high pressures and temperatures. *Phys. Rev. B* **53,** 8296–8309 (1996).
18. Gülseren, O., Cohen, R. E. & Krakauer, H. Equation of state and elasticity of Ta at high pressure. *Bull. Am. Phys. Soc.* **44,** 1490 (1999).
19. Huang, E., Bassett, W. A. & Tao, P. Pressure-temperature-volume relationship for hexagonal close packed iron determined by synchrotron radiation. *J. Geophys. Res.* **92,** 8129–8135 (1987).
20. Funamori, N., Yagi, T. & Uchida, T. High-pressure and high-temperature in situ x-ray diffraction study of iron to above 30 GPa using MA8-type apparatus. *Geophys. Res. Lett.* **23,** 953–956 (1996).
21. Alfé, D., Gillan, M. J. & Price, G. D. The melting curve of iron at pressures of the Earth's core from *ab initio* calculations. *Nature* **401,** 462–464 (1999).
22. Singh, S. C., Taylor, M. A. J. & Montagner, J. P. On the presence of liquid in Earth's inner core. *Science* **287,** 2471–2474 (2000).
23. Yoshida, S., Sumita, I. & Kumazawa, M. Growth model of the inner core coupled with outer core dynamics and the resultant elastic anisotropy. *J. Geophys. Res.* **101,** 28085–28103 (1996).
24. Dziewonski, A. M. & Anderson, D. L. Preliminary reference Earth model. *Phys. Earth Planet. Inter.* **25,** 297–356 (1981).
25. Bergman, M. I. Measurements of elastic anisotropy due to solidification texturing and the implications for the Earth's inner core. *Nature* **389,** 60–63 (1997).
26. Jeanloz, R. & Wenk, H.-R. Convection and anisotropy of the inner core. *Geophys. Res. Lett.* **15,** 72–75 (1988).
27. Wenk, H.-R., Matthies, S., Hemley, R. J., Mao, H.-K. & Shu, J. The plastic deformation of iron at pressures of the Earth's inner core. *Nature* **405,** 1044–1046 (2000).
28. Buffett, B. A. Geodynamic estimates of the viscosity of the Earth's inner core. *Nature* **388,** 571–573 (1997).
29. Karato, S.-I. Seismic anisotropy of the Earth's inner core resulting from flow induced by Maxwell stresses. *Nature* **402,** 871–873 (1999).
30. Buffett, B. A. & Wenk, H.-R. Texturing of the Earth's inner core by Maxwell stresses. *Nature* **413,** 60–63 (2001).

···

Texturing of the Earth's inner core by Maxwell stresses

B. A. Buffett* & **H.-R. Wenk†**

* *Department of Earth & Ocean Sciences, University of British Columbia, Vancouver, V6T 1Z4 Canada*
† *Department of Earth & Planetary Science, University of California, Berkeley, California 94720, USA*

···

Elastic anisotropy in the Earth's inner core has been attributed to a preferred lattice orientation[1], which may be acquired during solidification of the inner core[2] or developed subsequent to solidification as a result of plastic deformation[3–5]. But solidification texturing alone cannot explain the observed depth dependence of anisotropy[6–8], and previous suggestions for possible deformation processes have all relied on radial flow, which is inhibited by thermal[9] and chemical stratification[10]. Here we investigate the development of anisotropy as the inner core deforms plastically under the influence of electromagnetic (Maxwell) shear stresses. We estimate the flow caused by a representative magnetic field using polycrystal plasticity simulations for ε-iron, where the imposed deformation is accommodated by basal and prismatic slip[11]. We find that individual grains in an initially random polycrystal become preferentially oriented with their